Influence of alumina porosity and glass phase content on the microstructure and mechanical properties of metallized ceramics obtained by a Mo-Mn method

Ling Wang[1], Wen-tao Kang[2], Peng-zhao Gao[1*], Xiao-pan Liu[1], Evgeny V. Rebrov[3]

[1.]College of Materials Science and Engineering, Hunan University, Changsha, Hunan 410082, China;

[2] Loudi City Andeans Electronic Ceramics Co., Ltd. Loudi, Hunan 417000, China;

[3]School of Engineering, University of Warwick, Coventry, CV4 7AL, U.K;

Email address: gaopengzhao7602@hnu.edu.cn (Peng-zhao Gao)

Abstract: With the development of power electronics, metallizing of ceramics has been developed and employed in many industrial applications. This paper describes the effect of porosity, mean pore size and glass phase content of Al_2O_3 substrate on the microstructure evolution and mechanical properties of metallized ceramics obtained by an activated Mo-Mn method. The interface reaction as well as the joining strength between Al_2O_3 ceramic and Mo-Mn layer were investigated systematically using X-ray diffraction, SEM, energy dispersive X-ray analysis, et al. The overall porosity affects the 'absorptivity' of the substrate towards the glass phase in the metallized layer, while the glass phase content affects the diffusion depth of the Mn-containing phase. The results show that the distribution of the Mn-containing glass phase in the alumina substrate determined the failure characteristics of specimens under bending and tension conditions. The mean pore size determines the magnitude of capillary force responsible for the diffusion of Mn-containing glass phase into the ceramic substrate. The thickness of the Mo-Mn layer reduced and the thickness of the transition region increased at high alumina porosity. This resulted in a decrease of tensile strength, and an increase of flexural strength growth rate *GR* for specimens after metallization. The tensile strength of metallized specimens monotonously increased with the glass phase content, while the flexural strength first increased and then decreased. A tensile strength of 1990 ± 75 N, a flexural strength of 9499 ± 346 N and a He leakage rate of 3.5×10^{-11} $Pa\cdot m^3\cdot s^{-1}$ were obtained in the optimized specimens after metallization.

Keywords: Al_2O_3 ceramic metallization; porosity; glass phase content; metallization mechanism; mechanical properties; microstructure evolution.

1. Introduction

With the development of microelectronics technology, the complexity and the number of components in electronic devices are constantly increasing. The development of electronic packaging materials for components with excellent performance and satisfying various requirements has become a top priority [1, 2]. The ceramic-metal sealing technology was first studied in Germany in 1935, and Chinese research started in 1958 and was industrialized in 1975. At present, the technology is widely used in vacuum electronics, microelectronic packaging, energy industry, aerospace and other applications [3]. It is known that the difference in thermal expansion coefficient and elastic modulus between the ceramics and the metal results in a large residual stress at the ceramic-metal interface preventing strong connection between these materials [4]. Therefore, a metal layer must be sintered or deposited onto the surface of ceramics before the sealing process referred to as metallization [5]. Many ceramics metallization methods were developed, such as activated molybdenum-manganese (Mo-Mn) method [6, 7], direct copper method [8, 9], active metal brazing method [10, 11], magnetron spurring method [12,13]. The properties of the metallization layer directly affect the bonding strength, leakage rate and thermal cycle performance of the final ceramic-metal sealing products [14].

Ceramics is commonly composed of crystalline and glass phases with some porosity between them. Thus, the microstructure and related properties of ceramics after the metallization process depend on the amount and compositions of both phases, the pore size and the total pore volume [15, 16]. These parameters determine the bonding strength between the ceramic and the metal. Among all ceramics, alumina (Al_2O_3) was widely used in the ceramic-metal sealing process because of its high mechanical and electrical insulation strength, high wear and heat shock resistance, good hardness and chemical stability. It is an abundant and rather cheap raw material which can easily be manufactured [17, 18].

The activated Mo-Mn method is widely used at industrial scale for ceramic metallizing due to its high efficiency and reliability [19]. The process mainly includes the following two steps [20]. Initially, a Mo-Mn slurry is coated onto the surface of a polished alumina substrate by screen printing. Then, the coated alumina substrate is sintered to reduce the residual thermal stress and to improve the bonding strength between the ceramic and the metal. Twentyman [21] enhanced the tensile

strength by 59% from 44 to 70 MPa when sintering temperature on an alumina substrate was increased from 1400 to 1500 ^{o}C. The insufficient migration of glass phase from the alumina results in a weak sealing. After metallization with fine Mo particles, a more porous alumina with a 94% purity has a tensile strength by 20 MPa higher than that of alumina materials with 95% and 97% purity. In the Mo-Mn method, the adhesion of metallized layer onto the alumina surface increased with temperature. Also, the nanohardness of the metal-ceramic interface increased from 2.0 to 3.1 GPa in the process performed at higher temperature due to improved glass migration from the interface to the bulk material [22]. The tensile strength of the ceramic-metal interface was further improved by some additions in the slurry to enhance the glass diffusion. Intergranular failure via dynamic bending was identified as the main fracture mechanism of a ceramic-metal joint. However, a mixed transgranular/intergranular failure mechanism was observed for the quasi-static case. The crack originated from voids in the ceramic substrate and then expanded along the metallization band between solder and ceramics [23]. Lin [24] used active metallic brazing to deposit a thin Ti layer on the alumina surface. They studied the influence of the Ti layer and the porosity on the interfacial chemistry and microstructure evolution.

In this paper, influence of glass phase content, porosity and pore size of Al_2O_3 substrate on the microstructure evolution and mechanical properties of metallized ceramics obtained by a Mo-Mn method are presented. The metallized mechanism was discussed under the experiment condition.

2 Experimental

2.1 Raw Materials

Al_2O_3 powder (nominal size ~ 3.94 μm, purity ≥ 99 wt.%), $CaCO_3$ powders (nominal size ~14.1 μm, purity ≥ 99 wt.%), SiO_2 powder (nominal size~6.8 μm, purity ≥ 99 wt.%), kaolin powders (nominal size ~ 5.1 μm, purity ≥ wt.99 %) were all commercially obtained from Antaeus Company, Loudi, Hunan Province China, Carbon powder (nominal size~1.5 μm, purity ≥ 99 wt.%) was obtained from Yanming Material Co., Ltd. Liaocheng City, Shandong Province China, Where Al_2O_3 powder works as the main composition, $CaCO_3$, SiO_2 and kaolin as the glass phase former, carbon powder as the pore former.

The metallized slurry was mainly composed of molybdenum powder (≤ 2.5 μm, purity ≥ 99 wt.%), manganese powder (≤50 μm, purity ≥ 99 wt.%), and was commercially obtained from Zhuzhou Cemented Carbide Group, Zhuzhou, Hunan Province China. The additives of Al_2O_3, $CaCO_3$, SiO_2, kaolin powders, terpineol (C.P.) and ethyl cellulose ethoce (C.P.) were added in the slurry to make pastes (P-0.8, till P-10.6, Table 1) with desired viscosity. These resulted in materials with different porosity and glass phase contents after metallization. The respective sample codes are listed Table 1.

Please insert Table 1 here.

2.2 Preparation process

First, Al_2O_3, $CaCO_3$, SiO_2, kaolin and C powders were mixed in the desired ratios [25]. The mixture was ball milled, dried and compacted into ring-shaped specimens (o.d. 25 mm, i.d. 17.5 mm, thickness: 6 mm) under 100 MPa pressure for 60 s. Also alumina bars with a size of 40 mm (length) ×5 mm (width) × 5 mm (height) were prepared for mechanical properties measurements. All samples were sintered at the temperature in the range of 1500-1600 ^oC for 1 h to obtain alumina ceramics with different porosity and glass phase content [26]. After sintering, the ceramics was polished to obtain the surface roughness better than 1.6 μm. Then the premade metal-containing slurry was deposited to the upper and lower surfaces of the alumina rings by the screen printing method. The coated samples were dried in an oven at 80 ^oC for 2 h and then were sintered at 1500-1600 °C for 2 h in a tube furnace under N_2-H_2 atmosphere [27].

2.3 Characterization

The apparent porosity and pore volume of the as-prepared materials were measured via Archimedes method [28]. The closed porosity and relative density of these specimens were calculated according to the mixture rule. The pore size distribution was determined by mercury porosimetry (MIP, Pore Master-60, Quantachrome). The microstructure was observed with a Scanning Electron Microscope (SEM, FEI Quanta 200). The composition analysis before and after metallization was performed with Energy Dispersive X-ray spectroscopy (EDS, TN-4700). The glass phase content in the alumina was measured by the etching method [29]. The phase composition of

the metallized layer on the alumina surface was determined by XRD (X'Pert, PRO) with nickel filtered Cu K_α radiation produced at 40 kV and 27.5 mA, at a scanning rate of 5^o 2-theta/min. A leakage rate test was performed with a He Mass Spectrometer Leak Detector (ZQJ-2000, Beijing Zhongke Keyi Co., Ltd., China) following the method described in [30].

The mechanical properties of metalized specimen (alumina substrates coated with the Mo-Mn layer) were measured as follows. The flexural strength (σ_f) was determined with an automatic tension machine (CMT4300 30KN) with a speed of 0.2mm·min^{-1} [24]. The tensile strength (σ_t) was measured with an automatic tension machine (CMT4300 30KN) with a speed of 0.2mm·min^{-1}. Prior to this test, the sample was brazed to a copper-alloy bar. Both σ_f and σ_t before and after metallization were measured according to Ref [31].

The Microhardness was measured and an HX-1000TM/LCD instrument (Shanghai Optical Instrument Factory, China). For comparison, the flexural strength of the Al_2O_3 bar was determined via three point bending method in a span of 24 mm at a crosshead speed of 0.5 mm·min^{-1} using a universal material testing machine (INSTRON-3382). The specimens were polished prior to the respective mechanical properties testing. All tests were performed at room temperature. A batch of five identical samples was tested in every measurement and the average value is reported.

3 Results and discussion

3.1 Effect of substrate porosity on the microstructure evolution and mechanical properties variety of metallized specimens

3.1.1 Microstructure evolution of ceramics metallized specimens

The apparent porosity of ceramic substrates has a major influence on the metallization process [32]. The mechanical properties and pore size of five alumina substrates prepared with different porosity are listed in Table 2.

Please insert Table 2 here.

It can be seen from Table 2, that, the apparent porosity increases with the mean pore size while the flexure strength decreases. This behavior is in line with the results reported in [33]. Figure 1 (a-d)

show the microstructure of Al_2O_3 substrate before and after metallization, as well as the corresponding EDX spectra after metallization.

It can be seen in Fig.1a that the metal slurry forms a uniform layer with a thickness of 22 μm on the surface of alumina., After the metallization process, the Mo-Mn layer (white region in Fig.1b) is attached to the alumina surface (dark gray area), and a discontinuous glass phase (dark gray area) forms between the Mo-Mn layer and the alumina substrate [34]. The Mo-Mn layer thickness was measured in four metallized samples with different apparent porosity of alumina substrate (Fig.1 c-f, respectively). As the porosity increases, the layer thickness (including the Mo-Mn layer and the transition region) increases. However at a porosity of 6.58%, the thickness of metallized layer is still below than that of the initial metal slurry layer. It should also be mentioned that the thickness of the Mo-Mn layer decreases while that of the transition region increases at higher alumina porosity. This suggests that the transport of the metal-containing glass phase into the ceramic substrate during the metallization process occurs by diffusion at the boundaries between them. Therefore this can be seen as unidirectional diffusion. The larger the pore size of alumina, the higher the diffusion rate, which increases the thickness of the transition layer and reduces the thickness of the remaining Mo-Mn layer on the alumina surface.

Please insert Figure 1 here.

3.1.2 Study of mechanical properties of metallized ceramics

Figure 2 shows the flexural strength (σ_f) and tensile strength (σ_t) of alumina substrates with different apparent porosity before and after metallization. It can be seen that both σ_f and σ_t decrease for ring specimens from 1990 and 9499 N to 1485 and 1165 N, respectively, with the increase of alumina porosity from 0.77 to 6.58 % (Fig.2a). The value of *GR* increases from 65 to 81%, suggesting that the higher alumina porosity improves the mechanical properties of these specimens (Fig.2b). The higher the porosity, the greater the improvement of the mechanical properties.

Fracture of ceramics happens due to cleavage of Al-O, Ca-O, Mg-O and Si-O bonds. Previous studies showed that the presence of surface defects and enhanced porosity does not always improve mechanical properties [35]. In this study, the metallied layer modifies the alumina surface via two processes: (i) the diffusion of the ceramics glass phase into the interphase layer and (ii) the diffusion

of metal-containing glass phase into the porous network of alumina. The porosity of ceramic matrix is high and the strength of ceramics is low. However, because of the high porosity, the glass phase in the metallized layer permeates more into the ceramic layer after metallization sintering, and the bond energies of Al-O, Ca-O, Mg-O and Si-O are increased. As a result, the flexural strength of the metallized samples is greatly increased, so the flexural strength of the matrix with high porosity is higher than that of the ceramic matrix with low porosity [36]. The metallized layer also helps to improve the flexural strength of alumina.

Please insert Figure 2 here.

3.2 Effect of phase composition on the microstructure evolution and mechanical properties of metallized ceramics

3.2.1 Microstructure evolution of the metallized ceramics

The quality of metallization process depends on the chemical composition and the amount of glass phase in the ceramics [37]. The glass phase contains CaO-SiO_2 entities derived from the raw materials $CaCO_3$, SiO_2 and kaolin powder [38]. Initially, there are no differences between the glass and crystalline phases (Fig. 3a). Therefore the alumina substrates were etched to remove the glass phase (Fig. 3b). After etching, particles have an irregular polyhedral or plate-like shape with a size between 2 and 6 μm. The particles were interconnected via the sintering necks. The amount of glass phase was estimated by the weight difference before and after etching [21]. The physical properties of the samples are listed in Table 3.

Please insert Figure 3 here.

It can be seen that all alumina composites have a very low apparent porosity and the mean pore size remains essentially the same (4-5 μm). The flexure strength decreases with the increase of glass content.

Please insert Table 3 here.

The phase composition after metallization was confirmed by XRD measurements. The XRD patterns of three samples are shown in Figure 4. The main phase in all samples was α-Al_2O_3 (Hexagonal, JCPDF No.10-0173). The Mo metal (cubic, JCPDF No.42-1120) was minor phase with almost the same content in all three samples. However, the content of $MnAl_2O_4$ (cubic, JCPDF No.29-0880) increases at a higher glass phase content in sample G-9.6-M. The glass phase can be not detected [39].

Please insert Figure 4 here.

The possible reactions of Mn and Al_2O_3 are as follows [40]:

$$2Mn+O_2=2MnO \quad (1)$$

$$MnO+Al_2O_3=MnAl_2O_4 \quad (2)$$

Figure 5 shows the microstructure of a polished interface. The Mo-Mn layer can be seen between the bulk ceramics and Ag-Cu solder. The interface between the ceramics and the Mo-Mn layer has no visible voids, indicating a good wettability between metallized layer and the alumina surface. The elemental distribution maps are also presented. The metallized layer contains two phases: continuous Mo phase (white color) a discontinuous Mn-containing glass phase (gray color). The present of Al and Mo in the two adjacent phases is clearly seen in the elemental maps. This observation supports a previous conclusion, that a continuous Mo framework is important for a good connectivity between the ceramics and the Cu alloy bar [41]. The metallized layer near the Al_2O_3–metal interface is enriched with Mn (Fig. 5 (a3)). A higher Ni content is observed near the interface between the solder and the metallized layer which improves the fluidity of the Ag-Cu solder to wet the metallized layer and prevents that the metallized layer would be oxidized by the Cu alloy [42].

Please insert Figure 5 here.

The distribution of some key elements can help to identify the direction of element diffusion during the metallization process. The elemental distribution in different samples was measured with

EDS (Figure 6). The data are listed in Table 4. In the presence of CaO and SiO_2, several reactions (Eqs. 3-7) may occur in the sintering process and in the subsequent metallization process [43]. Yet, some of products cannot be detected by XRD due to their amorphous nature and/or low content.

$$6Al_2O_3 + CaO \rightarrow CA6 \quad (3)$$

$$CaO + SiO_2 \rightarrow CaSiO_3 \quad (4)$$

$$3CaO + 2SiO_2 \rightarrow Ca_3Si_2O_5 \quad (5)$$

$$CaO + Al_2O_3 + 2SiO_2 \rightarrow CAS2 \quad (6)$$

$$2CaO + Al_2O_3 + SiO_2 \rightarrow C2AS \quad (7)$$

Here, A, C, S represents Al_2O_3, CaO and SiO_2 respectively.

A combination of the XRD patterns (Figure 4) and EDS data (Table 4) allows to make some assumptions on the elemental and phase composition along the line from bulk alumina to the metal layer. These are based on the following observations and summarized in Table 4.

The alumina region near the interface is mainly composed of two phases, Al_2O_3 and C-S-A; In the Mo-Mn metal region, three phases are detected: Mo (white color), $MnAl_2O_4$ and CAS (light gray color) regardless of glass phase content in the alumina. The solder region is composed of Ag (white part) and Cu (gray part). In addition, the Mn content monotonously decreases from the bulk of the metallized layer to the alumina-metallized layer interface, regardless the content of glass phase. This confirms that the glass phase migrates from the metal layer to the ceramics during the metallization process.

Please insert Figure 6 here.

Please insert Table 4 here.

3.2.2 Mechanical properties of metallized ceramics

Before metallization, σ_f for rings decreases with the increase of glass phase content in Fig.7a, and the tensile strength of the metallized samples monotonously increases from 7683 to 10035 N with an increase of glass phase content from 1.0 to 9.5% in Fig.7b. In our experiments, the Mo-Mn layer and alumina have very similar composition to those reported in Ref [44] where it was shown that the

strength of interfacial bonds between the metallized layer and the ceramics is the main factor determining the tensile strength. As discussed above, the Mn-containing glass phase diffuses into the pore of alumina to form a new $MnAl_2O_4$ phase and the rate of this process increases with increasing the glass phase content. When a hexagonal alumina phase transforms into a more dense cubic $MnAl_2O_4$ phase, a higher density of Al-O and Mn-O bonds at the ceramics-metal interface can be realised. In the same way, the higher the glass phase content in the alumina, the larger the diffusion depth of the metal-containing glass phase, and the higher density of Mn-O bonds can be reached. The Mn-O bond energy of 656.56 $kJ \cdot mol^{-1}$ [45] is higher as compared to Al-O, which increases the tensile strength of the metallized alumina samples having higher glass phase content.

The flexural strength of the metallized samples first increases and then decreases with an increase of glass phase content. The highest value of 1990 N was observed in the sample with a medium content of glass phase. As it was discussed above, both the presence of surface defects and the pore volume would influence the flexural strength of ceramics. With the increase of glass phase content, the flexural strength of the alumina phase decreases. At the same time, the formation of $MnAl_2O_4$ phase occurs at much higher rate due to much faster diffusion of Mn into the alumina substrate. The latter helps to improve the flexural strength due to higher binding energy in the spinel phase as compared to that in the simple oxides (CaO, MgO). The resulting value for flexural strength is obtained as superposition of these two opposite trends and this results in an optimal value in the sample with a medium content of glass phase.

Please insert Figure 7 here.

3.2.3 Microhardness and leakage test of the metallized ceramics

The microhardness (Vicker hardness) on metallized specimens was measured at four positions along the line from bulk alumina to the solder region as show in Figure 8a. The corresponding values are shown in Figure 8b. The microhardness decreases when moving from the alumina via the Mo-Mn layer to the solder layer and then remains rather constant towards the Cu-bar. Such gradient helps to increase the adhesion and to enhance thermal shock resistance at the interface, allowing the joint to operate at higher temperatures [46, 47].

Please insert Figure 8 here.

An acceptable leakage rate range is less than 10^{-11} Pa·m^3·s^{-1}. The leakage rate of the metallized ceramics is listed in Table 5 [40]. The low porosity and higher glass phase content in samples G-4.8, G-7.6, G-9.5 are beneficial for the formation of a compact ceramics-metal layer interface, thus reducing the leakage rate of the material.

Please insert Table 5 here.

3.3 Metallization mechanism of ceramics

SEM images of the alumina surface before and after metallization are shown in Figure 9. In the initial sample, the microstructure of the metallized layer is relatively loose, and there are uniformly distributed small pores between the particles (Fig. 9a) or from the surface (Fig. 9c). After metallization, the microstructure of the metallized layer has undergone tremendous changes. Firstly, Mo particles bridge each other to form a skeleton structure, and there are quite a number of pores in the metallized layer. Also, the size and amount of pore on the surface of metallized layer is larger, and the average value of pore size is close to 1 μm (Fig. 9d).

Please insert Figure 9 here.

Many studies reported possible metallization mechanisms of Mo-Mn layer on an alumina substarte that involves several chemical and physical processes, such as the formation of new compounds, plastic flow of matter, and particle rearrangement [48, 49]. Based on the previously reported results and the new insights obtained in this study, we suggest a possible metallization mechanism as follows [50].

Prior to the process, the slurry, containing a certain amount of organic binder, plasticizers and Mo、Mn metal particles, was deposited onto the alumina surface (re-plotted Figure 10a, similar to Figure 1a). As the temperature increases, the organic binder was slowly oxidized in a reducing atmosphere containing a small amount of water vapors. Then the Mn (orange particles) metal was oxidized to

form MnO or Mn_3O_4 (red particles) in Fig. 10b [39]. When the temperature reaches the value by 50 -100 ℃ below the sintering temperature of metallization, a large volume of gases and voids was formed in the metallization layer. And there are a lot of liquid phases (red part) in metallized layer. As a result, the metallization layer shirked and the Mo particles were positioned in close contact to each other. Finally, a framework of Mo metal particle was formed. Because of the high viscosity of the mixture, the gas cannot escape from the solids and it is retained in the metallized layer between the Mo particles (Fig. 10c). The Mo framework structure is completely formed when the temperature reaches the metallization temperature (Fig. 10d). At the same time, the viscosity of the slurry decreases and two glass phases diffuse to each other under the action of capillary force. The metal-containing glass phase diffusion depth to the ceramics exceed that of ceramics to the metal layer. Thus, the metallized layer and the ceramic matrix form a firm combination. The migration of glass phase is the main mechanism of Mo-Mn metallization.

The capillary gravity P_{Mo} of glass phase in the metal layer is expressed by Eq (8) [21].

$$P_{Mo} = \frac{2T\cos\theta_{Mo}}{r} \tag{8}$$

where, T represents the surface tension of glass, θ_{Mo} is the wetting angle between glass phase and Mo metal, and r is the capillary radius in the metallized layer. In turn, the metal phase capillary gravity P_{Al2O3} into the ceramics is expressed by Eq (9) [51]:

$$P_{Al_2O_3} = \frac{2T\cos\theta_{Al_2O_3}}{R} \tag{9}$$

where θ_{Al2O3} is the wetting angle between glass phase and Al_2O_3, and R is the capillary radius in the ceramics.

Under experimental conditions, the composition and the particle size of the metal slurry remain the same, however the mean pore size increases with the increase of alumina porosity (Table 2). This reduces the capillary force (Equation 9). However, as we discussed above, the diffusion rate of Mn-containing glass phase, which results in the decrease of the Mo-Mn layer density, is also proportional to the pore volume. In fact, the superposition of these two factors determines that the thickness of metallized layer and the density of samples decreases with an increase of porosity, while the thickness of transition layer increases, resulting in an increase of fracture energy and in an increase of R value as shown in Fig. 2b.

The pore size of all samples and therefore the characteristic diffusion size is similar (Table 3). Thus, the diffusion rate is mainly determined by the content of glass phase in the alumina: the higher the glass content, the longer the diffusion length of Mn-containing phase resulting in a higher content of $MnAl_2O_4$ phase formed (as shown in Fig. 4) and reducing the thickness of the metallized layer (as shown in Fig. 6 and Table 4). Therefore the density at the alumina-metal interface increases and this leads to a higher value of σ_t (Fig. 7b), and a significant decrease in the leakage rate of He (as shown in Table 5).

Please insert Figure 10 here.

4 Conclusions

1) An increased porosity of ceramic substrate results in an increased pore size, which could reduce the capillary force when Mn-containing glass phase diffuses from metallized layer to Al_2O_3 substrate, meanwhile, higher porosity can supply higher space to 'absorb' the diffused glass phase, the combination of these two factors leads to an increased value of σ_f growth rate *GR* for specimens before and after metallization with the increase of the porosity, when porosity is 6.58% and pore diameter is 13.63 μm (specimen P-6.6-M), *GR* is up to 81%, while that of He leakage rate decreases to 430 $\times 10^{-11}$ $Pa \cdot m^3 \cdot s^{-1}$;

2) When ceramic substrates possess similar porosity and pore size of, diffusion behavior of Mn-containing glass phase is mainly affected by the content of glass phase in substrates, the higher the content of glass phase, the longer the diffusion path of Mn-containing glass phase in substrates, which results in an increase of $MnAl_2O_4$ content and σ_t of the specimen after metallization, when content of glass phase in ceramic substrate is 9.5 vol% (G-9.5-M), σ_t of specimen after metallized is up to 10035N, and He leakage rate decreases to 1.3×10^{-11} $Pa \cdot m^3 \cdot s^{-1}$;

3) During metallization process, the capillary force derived from the pore size of substrate mainly acts as the driving force for the diffusion of Mn-containing glass phase, and porosity of substrate can affects the 'absorptivity' of substrate to Mn-containing glass phase, while the glass phase content of substrate affects the diffusion depth of Mn-containing glass phase in the substrate. The

microstructure evolution and the mechanical properties variety of the metallized specimens are the result of the interaction of these three factors.

Conflicts of interest

There is no interest conflict with others.

Acknowledgement

This work is supported by the Natural Science Foundation of Hunan Province (2018JJ4011).

References

[1] R. Voytovych, F. Robaut, N. Eustathopoulos, The relation between wetting and interfacial chemistry in the CuAgTi/alumina system, Acta Mater. 54 (8) 2006 2205-2214.
[2] G.B. Niu, D.P. Wang, Z.W. Yang, Y. Wang, Microstructure and mechanical properties of Al_2O_3 ceramic and TiAl alloy joints brazed with Ag-Cu-Ti filler metal, Ceram. Int. 42 (6) 2016 6924-6934.
[3] L.Q. Gao, Practical sealing technology of ceramic-metal material, Chemisty Industry Press, 2005 1-11.
[4] K. Nogi, The role of wettability in metal-ceramic joining, Scripta Mater. 62 (12) 2010 945-948.
[5] Y. Ma, D.Wang, G. Ren, Progress of research on the alumina ceramics metallization, Vac. Electron. 5 2007 41-43.
[6] D. Kuo, K. Yeh, R. Shiue, M. Wei, Microstructural characterizations of the 316 stainless steel-alumina joining by a modified Moly-Manganese process and brazing, Adv. Mater. Res. 189-193 2011 3339-3344.
[7] K. White, D. Kramer Microstructure and seal strength relation in the Molybdenum- Manganese glass metallization of alumina ceramics, Mater. Sci. Eng. 75 (1-2) 1985 207-213.
[8] K. Hromadka, J. Stulik, J. Reboun, A. Hamacek, DBC technology for low cost power electronic substrate manufacturing, Procedia Eng. 69 (1) 2014 1180-1183.
[9] L. Xu, M. Wang, Y. Zhou, Z. Qian, S. Liu, An optimal structural design to improve the reliability of Al_2O_3-DBC substrates under thermal cycling, Microelectron. Rel. 56 (6) 2016 101-108.
[10] Niu G B, Wang D P, Yang Z W, Wang Y, Microstructure and mechanical properties of Al_2O_3/TiAl joints brazed with B powders reinforced Ag-Cu-Ti based composite fillers, Ceram. Int. 43 (1) 2017 439-450.
[11] Z. Zhong, G. Hou, Z. Zhu, Z. Wang, G. Wang, Y. Wu, Microstructure and mechanical strength of SiC joints brazed with Cr_3C_2, particulate reinforced Ag-Cu-Ti brazing alloy, Ceram. Int. 44 (10) 2018 11862-11868.
[12] J. Dy-Lim, P. Mun-Lee, D. Min-Woo-Rhee, K. Chew-Leong, Z. Chen, Effect of surface treatment on adhesion strength between magnetron sputtered copper thin films and alumina substrate, Appl. Surf. Sci. 355 2015 509-515.
[13] S. Anwar, S. Anwar, P. Nayak, Multilayer composite ceramic-metal thin film: Structural and mechanical properties, Surf. Interface, 10 2018 110-116.

[14] Z. Cai, C. Zhang, R. Wang, C. Peng, X. Wu, H. Li, High-temperature mechanical properties and thermal cycling stability of Al-50Si alloy for electronic packaging, Vac. Sci. Technol.A 728 2018 95-101.
[15] L.Q. Gao, Glass phase and ceramic metallizing technology, Vac. Electron. 4 2013 79-83.
[16] L. Fu, A. Huang, H. Gu, H. Ni, Properties and microstructures of lightweight alumina containing different types of nano-alumina, Ceram. Int. 44 (15) 2018 17885-17894.
[17] M. Michalek, M. Michalkov, G. Blugan, J. Kuebler, Strength of pure alumina ceramics above 1 GPa, Ceram. Int. 44 (3) 2018 3255-3260.
[18] S.B. Dhuban, S. Ramesh, C.Y. Tan, Y.H. Wong, U. Johnson Alengaram, S. Ramesh, W.D. Teng, F. Tarlochan, U. Sutharsini, Sintering behaviour and properties of manganese-doped alumina, Ceram. Int. 45 2019 7049-7054.
[19] S. H. Yang, S. Kang, Fracture behavior and reliability of brazed alumina joints via Mo–Mn process and active metal brazing, J. Mater. Res. 15 (10) 2000 2238-2243.
[20] G. Liu, G. Qiao, H.Wang, Z. Jin, Microstructure and strength of alumina-metal joint brazed by activated Molybdenuma-Manganese method, Key Eng. Mater., 353-358 2007 2049-2052.
[21] M. E. Twentyman, P. Popper, High-temperature metallizing: Part 2 The effect of experimental variables on the structure of seals to debased aluminas, J. Mater. Sci. 10 1975 777-790.
[22] S. Ghosh, A. Sengupta, K.S. Pal, N. Dandapat, R. Chakraborty, S. Datta, D. Basu, Characterization of metallized alumina ceramics, Metall. Mater. Trans. A, 43 (3) 2012 912-920.
[23] K. Lin, M. Singh, R. Asthana, Interfacial characterization of alumina-to-alumina joints fabricated using silver-copper-titanium interlayers, Mater. Charact. 90 2014 40-51.
[24] L. Li, W. Guo, X. Yu, D. Fu, Mechanical behavior of ceramic-metal joint under quasi-static and dynamic four point bending: Microstructures, damage and mechanisms, Ceram.Int. 43 2017 6684-6692.
[25] F. Dohler, T. Zscheckel, S. Kasch, T. Schmidt, C. Russel, A glass in the $CaO/MgO/Al_2O_3/SiO_2$ system for the rapid laser sealing of alumina, Ceram. Int. 43 (5) 2017 4302-4308.
[26] R. Zhang, S. FU, H. Lu, H. Xu, J. Liu, H.Z, The effects of the sintering schedule on the properties of the alumina ceramics, Vac. Electron. 4 2004 42-44.
[27] Sergey V. Komarov, Sergey E. Romankov, Mechanical metallization of alumina substrate through shot impact treatment, J. Eur. Ceram. Soc. 34 (2) 2014 391-399.
[28] K. Madhav-Reddy, B. Prasad-Saha, Effect of porosity on the structure and properties of β-SiAlON ceramics, J. Alloys Compd. 779 2019 590-598.
[29] W. Guo, H. Xiao, X. Yao, J. Liu, J. Liang, P. Gao, G. Zeng, Tuning pore structure of corrosion resistant solid-state-sintered SiC porous ceramics by particle size distribution and phase transformation, Mater. Des., 100 2016 1-7
[30] P. Mishra, P. Sengupta, S.N. Athavale, A.L. Pappachan, A.K. Grover,A.K. Suri, G.B. Kale, P.K. De, K. Bhanumurthy, Brazing of hot isostatically pressed-Al_2O_3 to stainless steel (AISI 304L) by Mo-Mn route using 72Ag-28Cu braze, Metall. Mater. Trans. A, 36 (6) 2005 1487-1494.
[31] G. Liu, G. Qiao, H. Wang, Z. Jin, Microstructure and strength of alumina-metal joint brazed by activated Molybdenuma-Manganese method, Key Eng. Mater. 353-358 2007 2049-2052.
[32] Cui Z, Huang Y, Liu H, Predicting the mechanical properties of brittle porous materials with various porosity and pore sizes, J. Mech. Behav. Biomed. 71 2017 10-22.
[33] R. W. Rice, Evaluating porosity parameters for porosity–property relations, J. Am. Ceram. Soc. 76 (7) 1993 1801-1808.

[34] Y. Song, D. Liu, S. Hu, X. Song, Y. Lei, J. Cao, Brazing of metallized SiC ceramic to GH99 superalloy using graphene nanoplatelets reinforced AgCuTi composite filler, Ceram. Int. 45 (7) 2019 8962-8970.
[35] Y. Jing, X. Deng, J. Li, C. Bai, W. Jiang, Influence factors on the porosity and strength of SiC/mullite composite porous ceramics, Bull. Chin. Ceram. Soc. 32 (10) 2013 1979-1983.
[36] Y. Huang, A. Cai, Y. Liu, Y. Liu, H. Liu, Various components of activating agent for molybdenum manganese metallization play the role in the formulation, Vac. Electron. 4 2008 42-45.
[37] J. Zhu, X. Pu, Glass phase in high-alumina ceramics, Vac. Electron. 1 2003 56-57.
[38] J. Bai, H. Li, Z. Zhang, H. Wei, J. Jun, H. Qu, Y. Xiao, The additives effect on the properties for alumina ceramic, Ceramics 10 2014 9-16.
[39] C. Xin, W. Liu, N. Li, J. Yan, S. Shi, Metallization of Al_2O_3 ceramic by magnetron sputtering Ti/Mo bilayer thin films for robust brazing to Kovar alloy, Ceram. Int. 42 (8) 2016 9599-9604.
[40] I. Foroutan, R. Sarraf-Mamoory, N. Hosseinabadi, Alumina-copper joining by the sintered metal powder process, Ceram. Int. 36 (2) 2010 741-747.
[41] Q. Li, P. Song, K. Lu, Q. Dong, Q. Li, J. Tan, Q. Li, J. Lu, Fracture behaviour of ceramic-metallic glass gradient transition coating, Ceram. Int. 45 (5) 2019 5566-5576.
[42] G. Liu, G. Qiao, Research progress on ceramic-metal seals via the activated molybdenum-manganese process, Vac. Electron. 34 (12) 2006 1522-1527.
[43] A. Cai , X. Chen, I. Cu, Y. Huang, Study on the metallization of high glass phase 95% Al_2O_3 ceramic, Vac. Electron. 4 2015 47-51.
[44] Z. Zheng, Y. Zhang, F. Yi, C. Chen, X. Song, Surface metallization of alumina ceramics: Effects of sintering time and substrate etching, Ceram. Int. 40 (8) 2014 12709-12715.
[45] H.T.Wu, Z.B.Feng, Q.J.Mei, J.D.Guo, J.X.Bi, Correlations of crystal structure, bond energy and microwave dielectric properties of $AZrNb_2O_8$ (A=Zn, Co, Mg, Mn) ceramics, J. Alloys Compd. 648 2015 368-373.
[46] S. Ghosh, K. Sundar-Pal, N. Dandapat, S. Datta, D. Basu, Interfacial properties of metallized alumina ceramics, Met. Mater. Int. 18 (4) 2012 625-630.
[47] F.J. Paneto, J.L. Pereira, J.O. Lima, E.J. Jesus, L.A. Silva, E. Sousa Lima, R.F. Cabral, C. Santos, Effect of porosity on hardness of Al_2O_3-$Y_3Al_5O_{12}$ ceramic composite, Int. J. Refract. Met. Hard Mater. 48 2015 365-368.
[48] Y. Lu, Discussion on the moly-manganese process for alumina ceramic, Vac. Electron. 4 2010 14-17.
[49] J. Zhang , L. Gao, Study on sintering mechanism of the metallized layers of 95 % Al_2O_3 ceramic in mo-mn process, Vac. Electron. 4 2007 6-9.
[50] R. M. D. Nascimento, A. E. Martinelli, A. J. A. Buschinelli, Recent advances in metal-ceramic brazing, Ceramica, 2003, 49:178-198.
[51] K. Zhao, Analysis on metalizing mechanisms of Al_2O_3-based ceramics by Molybdenum-Manganese route and related experimental results, Vac. Electron. 4 2010 24-29.

Figure Captions

Figure 1. Microstructure of as-prepared specimens before (a) and after metallization (b) and the correspond line scanning spectra of specimens after metallization with porosity of P-0.8-M (c), P-2.3-M (d), P-3.6-M (e), and P-6.6-M (f).

Figure 2. σ_f and σ_t of Al_2O_3 ring with different apparent porosity before after metallization.

Figure 3. SEM photographs of Al_2O_3 substrate before (a) and after corrosion (b).

Figure 4. XRD patterns of the metallized ceramics.

Figure 5. Microstructure of a polished cross section of Al_2O_3 substrate with metallized layer-Ni layer-solder layer-Cu alloy (a) and element distribution map (a1) Al; (a2) Mo; (a3) Mn; (a4) Ni; (a5) Ag; (a6) Cu.

Figure 6. Microstructure and interface EDS composition of metallized specimens with different glass phase content (a) G-1.0-M; (b) G-2.8-M; (c) G-4.8-M; (d) G-7.6-M; and (e) G-9.5-M.

Figure 7. Flexural and tensile strength of Al_2O_3 ring with different apparent porosity before after metallization.

Figure 8. (a) The microhardness measurement positions in the metallized sample and (b) the corresponding values as a function of the position.

Figure 9. SEM photographs of metallized layer before and after sintering a) Fracture surface of specimen before sintering; b) fracture surface of specimen after sintering; c) surface of specimen before sintering; d) surface of specimen after sintering.

Figure 10. Metallization mechanism of ceramics.

Table Captions

Table 1. Designed Al_2O_3 substrate with different porosity and glass phase contents.

Table 2. Mechanical properties of Al_2O_3 substrates with different porosity.

Table 3. Properties of alumina ceramics.

Table 4. Element content and assumed phases of each point marked in Figure 6 (at.%).

Table 5. Leakage rate of specimens after metallization.

Table 1 Designed Al_2O_3 substrate with different porosity and glass phase contents

Apparent Porosity (vol.%)*		0.77	2.31	3.55	6.58	10.63
Serial number	Ceramic substrate	P-0.8	P-2.3	P-3.6	P-6.6	P-10.6
	After metallization	P-0.8-M	P-2.3-M	P-3.6-M	P-6.6-M	P-10.6-M
Glass phase content (vol.%)		1.0	2.8	4.8	7.6	9.5
Serial number	Ceramic substrate	G-1.0	G-2.8	G-4.8	G-7.6	G-9.5
	After metallization	G-1.0-M	G-2.8-M	G-4.8-M	G-7.6-M	G-9.5-M

* Here, the glass phase content in Al_2O_3 substrate is 95 vol.%.

Table 2. Mechanical properties of Al_2O_3 substrates with different porosity

Specimen	P-0.8	P-2.3	P-3.6	P-6.6	P-10.6
Apparent porosity (%)	0.77	2.31	3.55	6.58	10.63
Volume density ($g \cdot cm^{-3}$)	3.72	3.53	3.42	3.31	3.17
Closed porosity (%)*	1.47	5.04	6.69	6.53	6.16
Pore size (μm)	4.49	5.66	10.33	13.63	18.72
Flexure strength (MPa, bar)	303.58 ±19.05	278.40 ± 27.88	243.47 ±44.28	224.43 ±58.94	180.23 ± 65.34**

* The theoretical density of 95%Al_2O_3 in this experiment is $3.81 g \cdot cm^{-3}$, data of the closed porosity are calculated via the mixture rule. ** σ_f of P-10.6 is too low and is abandoned.

Table 3. Properties of alumina ceramics

Specimen	Volume density ($g \cdot cm^{-3}$)	Apparent porosity (%)	Closed porosity (%)	Glass phase (vol.%)	Al_2O_3 content (wt.%)	Pore size (μm)	Flexure Strength (MPa)
G-1.0	3.78	0.84	1.74	1.0	98.9	5.32	376.74±27.88
G-2.8	3.69	0.82	3.09	2.8	97.1	5.25	321.59±35.93
G-4.8	3.72	0.77	1.59	4.8	95.2	4.49	303.58±19.05
G-7.6	3.64	0.98	1.93	7.6	92.3	4.63	273.87±49.94
G-9.5	3.6	0.86	2.10	9.5	90.4	5.72	250.91±11.19

* The theoretic density of G-1.0, G-2.8, G-4.8, G-7.6, G-9.5 specimens in this experiment is 3.88$g \cdot cm^{-3}$, 3.84$g \cdot cm^{-3}$, 3.81$g \cdot cm^{-3}$, 3.75$g \cdot cm^{-3}$, 3.71$g \cdot cm^{-3}$.

Table 4 Element content and assumed phases of each point marked in Figure 6 (at.%)

Specimen	Point	O	Mg*	Al	Si	Ca	Mo	Mn	Ni	Ag	Cu	Assumed Phase
	A1	46.75	0.46	51.51	0.36	0.69	0	0.11	0.12	0	0	Al_2O_3
	A2	45.35	0.36	52.90	0.25	0.26	0.39	0.30	0.19	0	0	Al_2O_3
G-1.0-M	A3	37.29	0.21	6.55	0.04	0.06	54.42	1.11	0.32	0	0	Mo, Al_2O_3(small amount)
	A4	44.57	0.23	39.98	0.41	0.08	10.32	2.92	1.49	0	0	$MnAl_2O_4$, Mo(small amount)
	A5	8.86	0	0	0	0	0.12	0	0	1.1	89.92	Cu, Ag(small amount)
	B1	37.51	0.21	57.53	2.32	1.96	0	0.16	0.31	0	0	Al_2O_3, CAS2(small amount)
	B2	36.95	0.27	58.66	1.96	1.28	0.16	0.35	0.37	0	0	Al_2O_3, CAS2(small amount)
G-2.8-M	B3	31.44	0.06	5.90	0.11	1.04	59.73	1.23	0.49	0	0	Mo, Al_2O_3(small amount)
	B4	31.32	0.71	55.7	0.5	5.32	1.82	2.77	1.86	0	0	$MnAl_2O_4$, C2AS(small amount)
	B5	6.93	0	0	0	0	0	0	0	1.47	91.6	Cu, Ag(small amount)
	C1	32.98	0.77	59.69	5.67	0.42	0	0.21	0.26	0	0	Al_2O_3, AS(small amount)
	C2	31.5	0.69	61.81	4.85	0.33	0.1	0.42	0.3	0	0	Al_2O_3, CS(small amount)
G-4.8-M	C3	30.06	0.34	13.9	0.46	0.13	53.56	1.26	0.32	0	0	Mo, Al_2O_3(small amount)
	C4	31.61	0.30	20.95	28.15	4.95	9.89	2.63	1.61	0	0	$MnAl_2O_4$, CAS2(small amount)
	C5	4.85	0	0	0	0	0	0	0	1.76	93.39	Cu, Ag(small amount)
	D1	34.52	0.32	50.01	9.82	4.97	0	0.24	0.12	0	0	Al_2O_3, CAS2(small amount)
	D2	33.98	0.27	51.79	8.68	4.39	0.2	0.5	0.19	0	0	Al_2O_3, CAS2(small amount)
G-7.6-M	D3	30.11	0.13	11.15	4.21	2.36	50.46	1.32	0.23	0	0	Mo, CSA(small amount)
	D4	29.40	0	20.26	18.98	14.75	12.33	2.54	1.74	0	0	$MnAl_2O_4$, CAS2(small amount)
	D5	4.36	0	0	0	0	0	0	0	2.32	93.32	Cu, Ag(small amount)
	E1	36.79	0.4	53.28	5.54	3.58	0	0.33	0.08	0	0	Al_2O_3, CAS2(small amount)
	E2	36.51	0.38	55.35	4.02	2.83	0.26	0.52	0.13	0	0	CAS2(small amount)
G-9.5-M	E3	35.06	0.13	16.03	5.53	5.91	35.79	1.43	0.12	0	0	Mo, CSA(small amount)
	E4	37.39	0.37	20.41	18.8	12.1	7.77	2.62	0.54	0	0	$MnAl_2O_4$, CAS2(small amount)
	E5	6.97	0	0	0	0	0	0	0	2.69	90.34	Cu, Ag(small amount)

* Small amount of Mg may derive from the raw mineral of kaolin.

Table 5 leakage rate of specimens after metallization

Serial number	P-0.8-M	P-2.3-M	P-3.6-M	P-6.6-M	G-1.0-M	G-2.8-M	G-4.8-M	G-7.6-M	G-9.5-M
Leakage rate ($Pa \cdot m^3 \cdot s^{-1}$, 10^{-11})	3.5	10.5	56	430	9.3	6.8	3.5	2.3	1.3

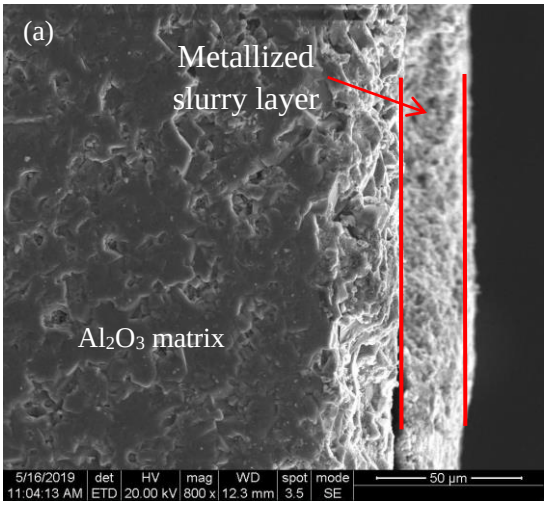

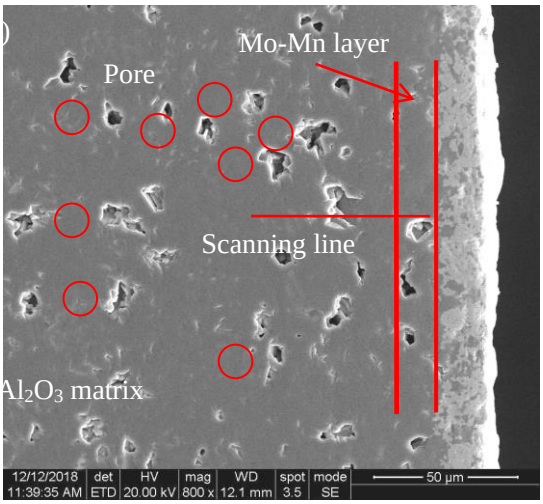

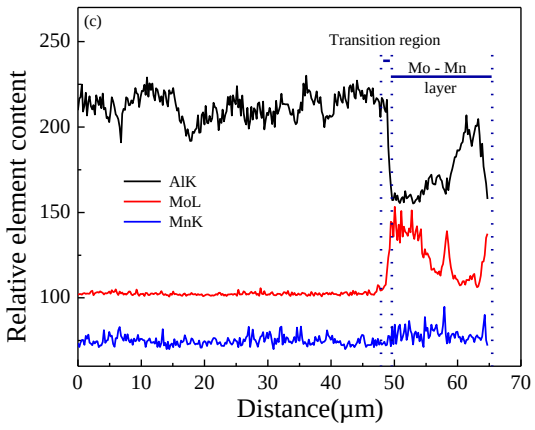

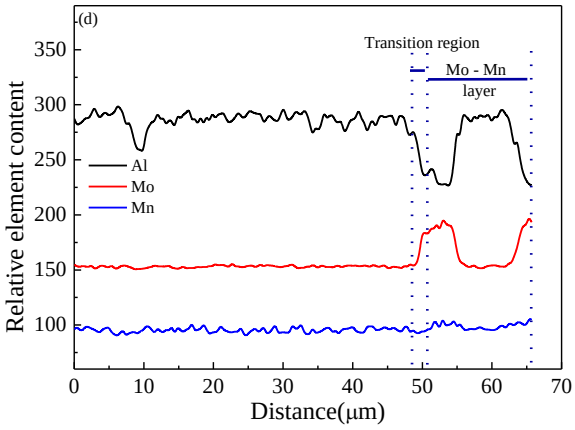

Mo-Mn layer 15.32 µm; Transition region 1.42µm

Mo-Mn layer 14.96 µm; Transition region 1.94µm

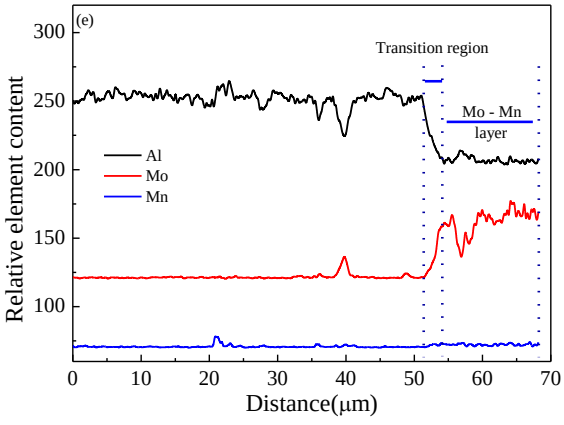

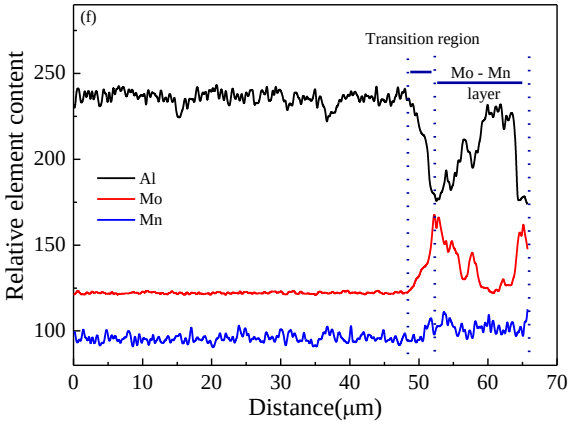

Mo-Mn layer 14.25 µm; Transition region 2.96µm

Mo-Mn layer 13.59 µm; Transition region 3.84µm

Figure 1 Microstructure of as-prepared specimens before (a) and after metallization (b) and the correspond line scanning spectra of specimens after metallization with porosity of P-0.8-M (c), P-2.3-M (d), P-3.6-M (e), and P-6.6-M (f).

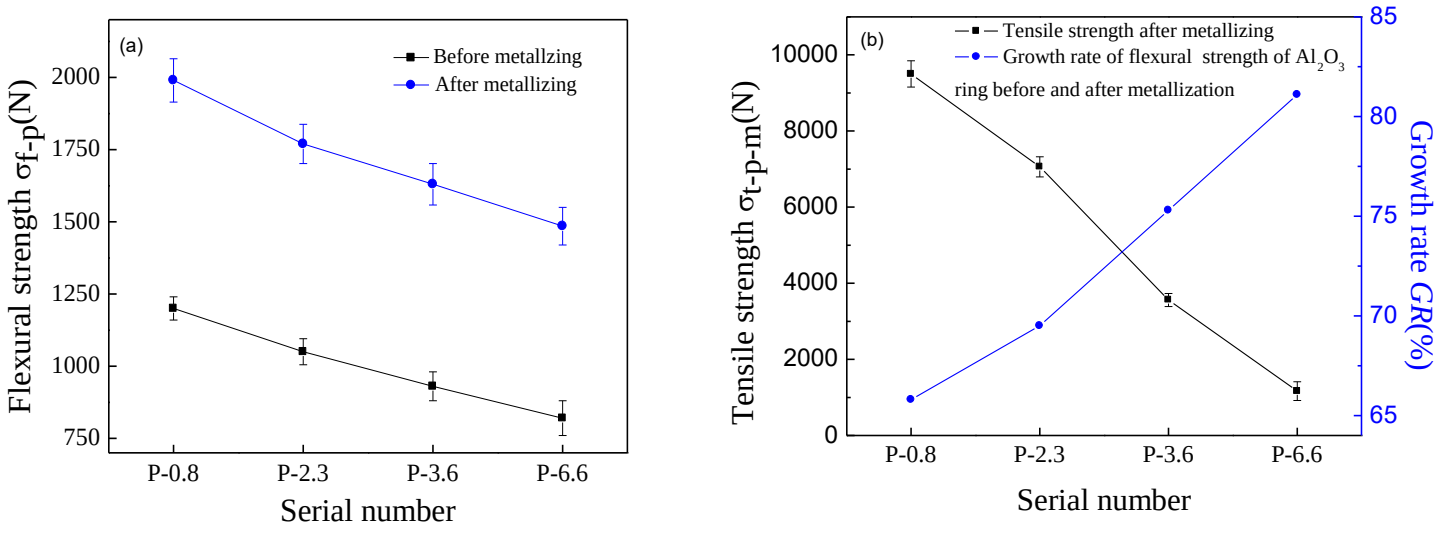

Figure 2 Flexural and tensile strength of Al_2O_3 ring with different apparent porosity before and after metallization

Ps: $\sigma_{f\text{-}p}$ stand for Flexural strength of Al_2O_3 ring; $\sigma_{f\text{-}p\text{-}m}$ stand for Flexural strength of Al_2O_3 ring after metallization; $\sigma_{t\text{-}p\text{-}m}$ stand for tensile strength of Al_2O_3 ring after metallization; $GR = (\sigma_{f\text{-}p\text{-}m} - \sigma_{f\text{-}p})/ \sigma_{f\text{-}p} \cdot 100\%$.

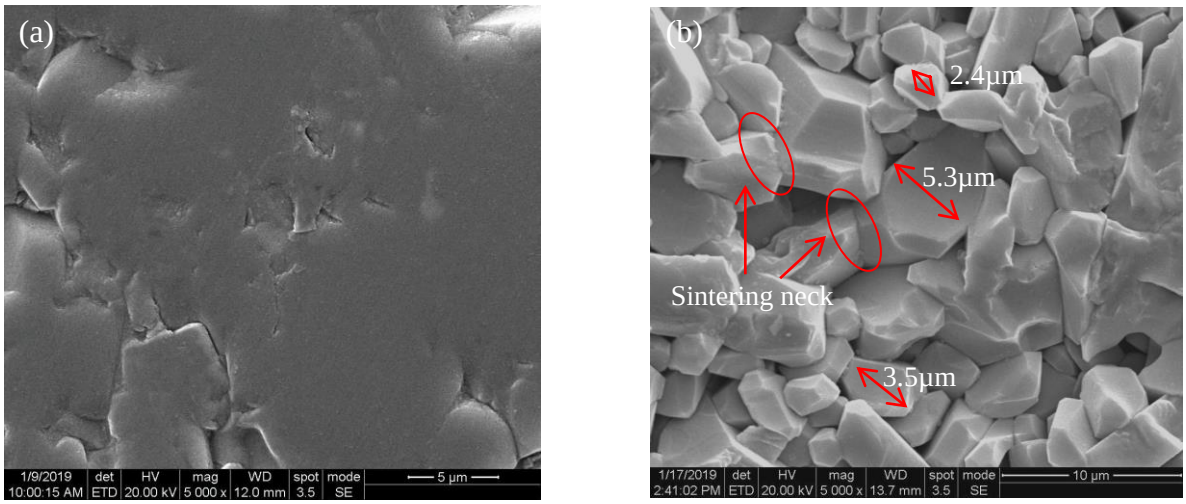

Figure 3 SEM photographs of Al_2O_3 substrate before (a) and after corrosion (b).

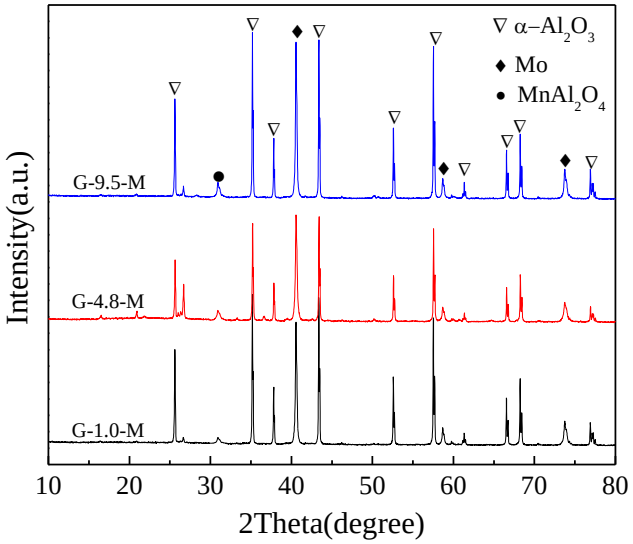

Figure 4 XRD patterns of the metallized ceramics.

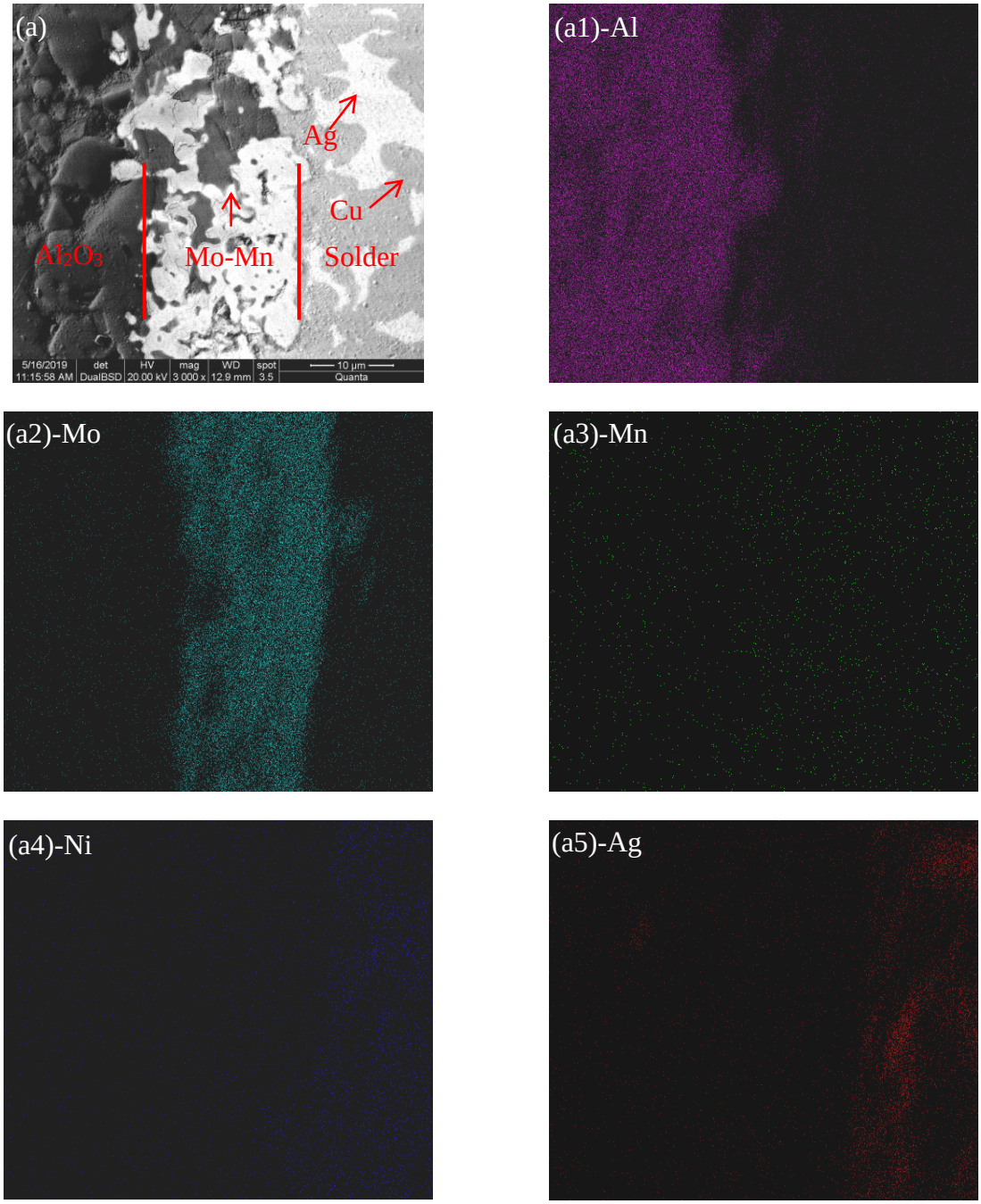

Figure 5 Microstructure of a polished cross section of Al_2O_3 substrate with metallized layer-Ni layer-solder layer-Cu alloy (a) and element distribution map (a1) Al; (a2) Mo; (a3) Mn; (a4) Ni; (a5) Ag; (a6) Cu.

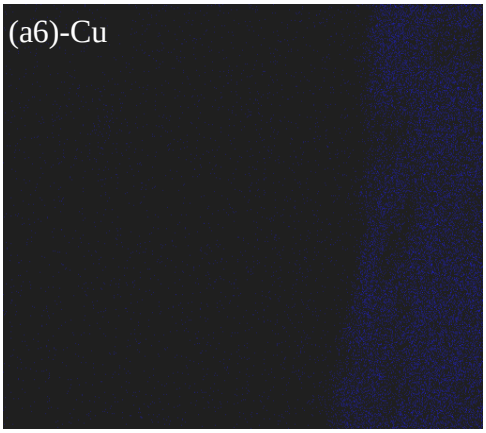
(a6)-Cu

.

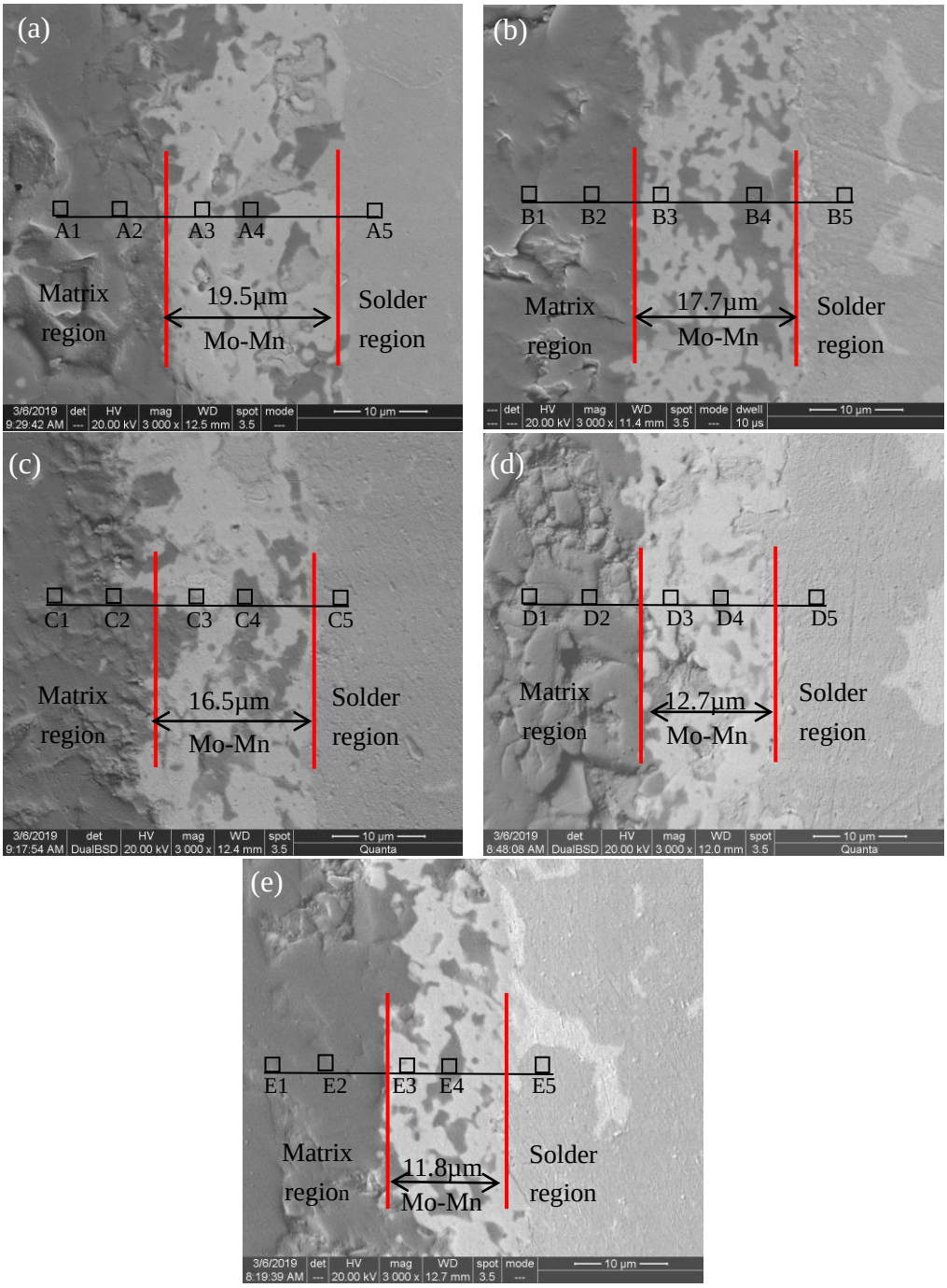

Figure 6 Microstructure and interface EDS composition of metallized specimens with different glass phase content (a) G-1.0-M; (b) G-2.8-M; (c) G-4.8-M; (d) G-7.6-M; and (e) G-9.5-M.

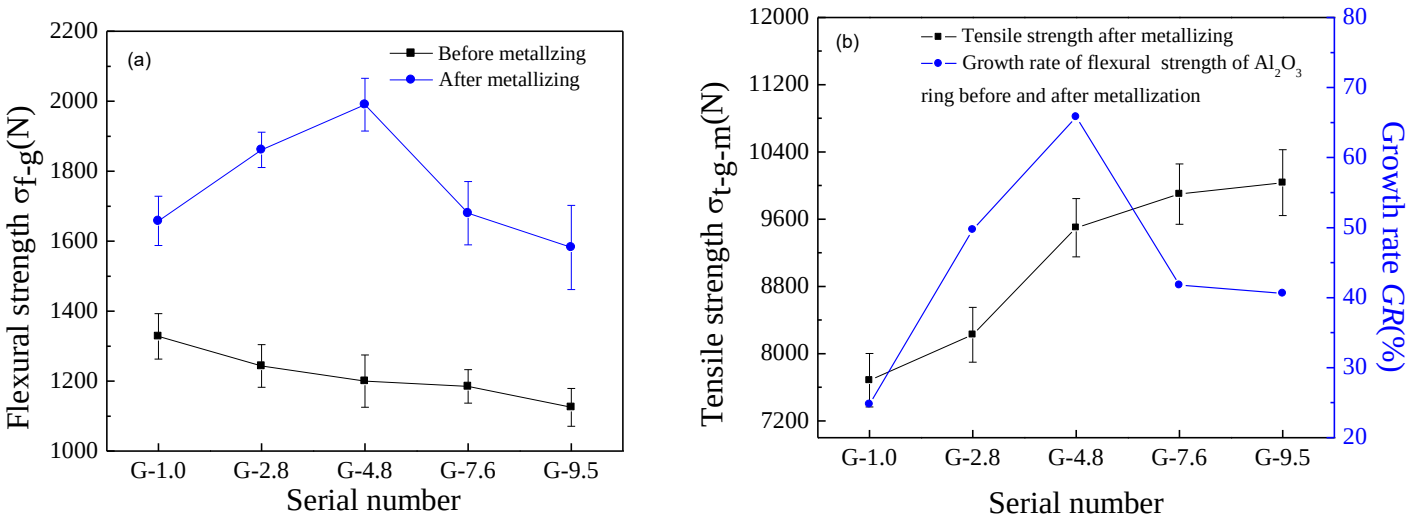

Figure 7 Flexural and tensile strength of Al_2O_3 ring with different content of glass phase before and after metallization

Ps: $\sigma_{f\text{-}g}$ stand for Flexural strength of Al_2O_3 ring; $\sigma_{f\text{-}g\text{-}m}$ stand for Flexural strength of Al_2O_3 ring after metallization; $\sigma_{t\text{-}g\text{-}m}$ stand for tensile strength of Al_2O_3 ring after metallization; $GR = (\sigma_{f\text{-}g\text{-}m} - \sigma_{f\text{-}g})/ \sigma_{f\text{-}g} \cdot 100\%$.

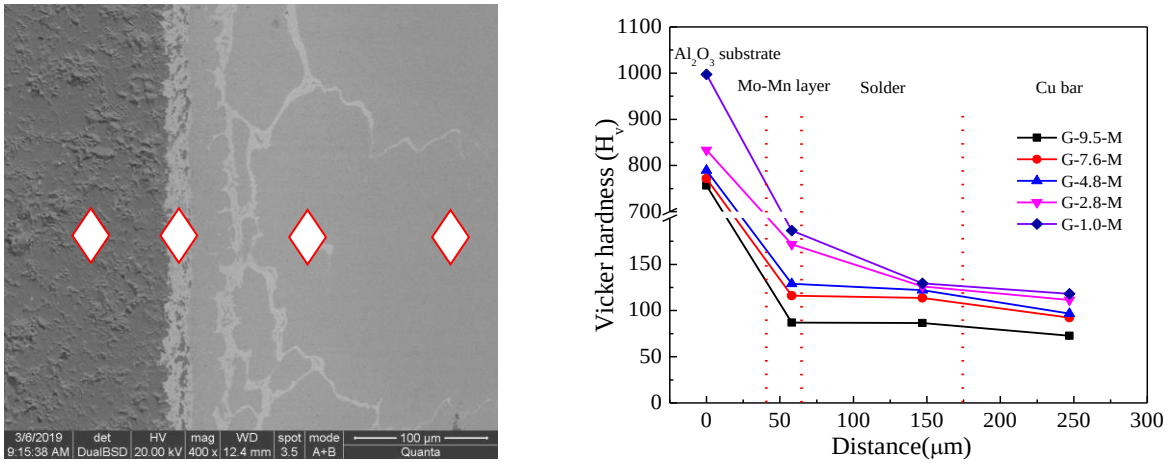

Figure 8 (a) The microhardness measurement positions in the metallized sample and (b) the corresponding values as a function of the position.

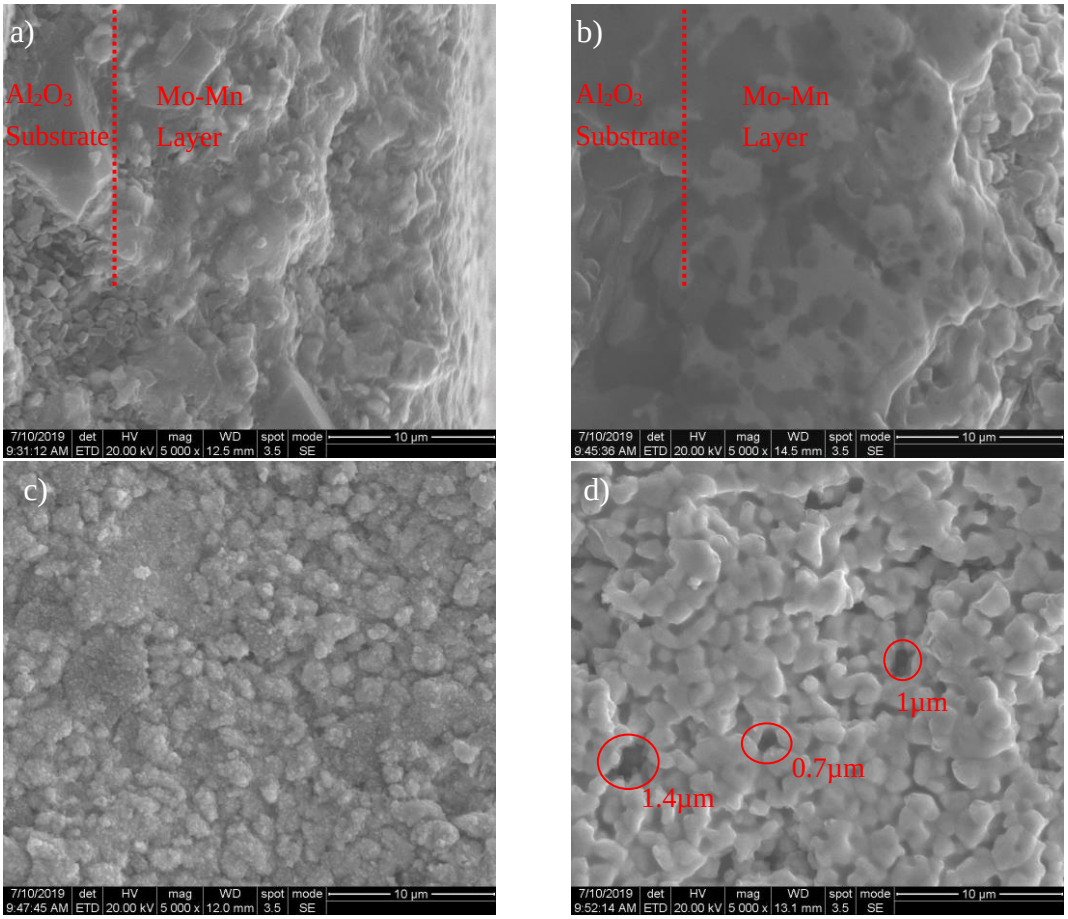

Figure 9 SEM photographs of metallized layer before and after sintering

a) Fracture surface of specimen before sintering; b) fracture surface of specimen after sintering;

c) surface of specimen before sintering; d) surface of specimen after sintering.

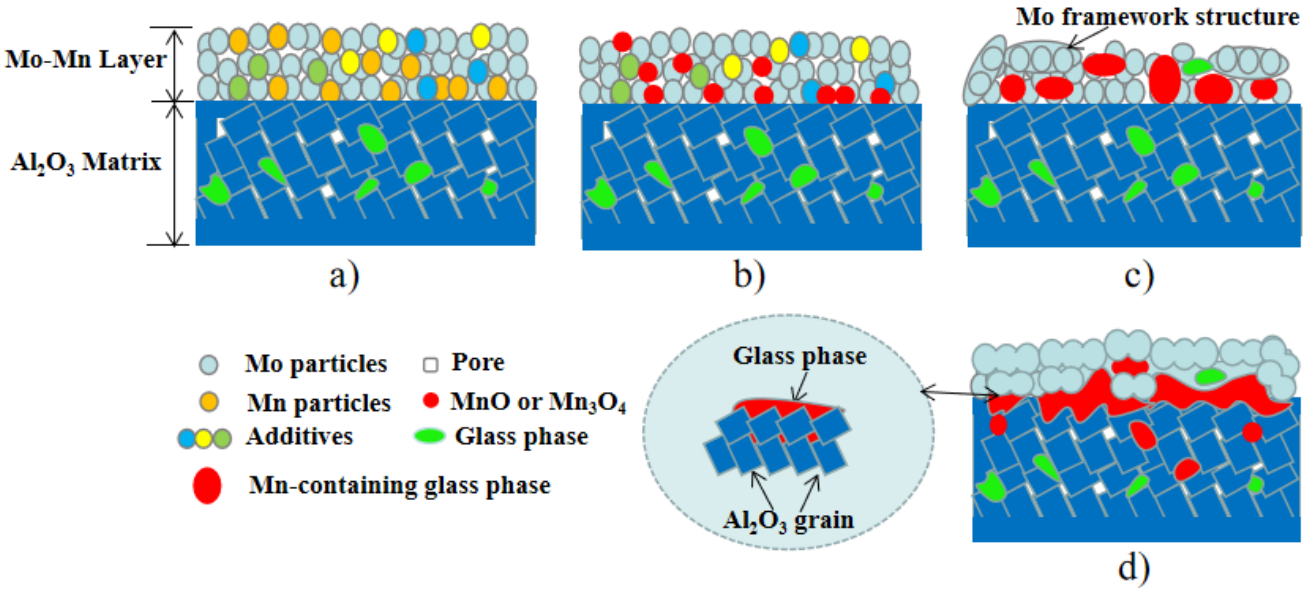

Figure 10 Metallization mechanism of ceramics.